MRS Communications (2026) 16:884–894
© The Author(s), under exclusive licence to The Materials Research Society, 2026
https://doi.org/10.1557/s43579-026-00955-6

MRS Communications

Research Letter

An aspect ratio–guided printing angle optimization framework for 3D-printed microneedles

Emre Ece, Shammas Mohamed, Eylul Gulsen Yilmaz, Dilsad Taydas, Nedim Hacıosmanoğlu, and Fatih Inci, UNAM-National Nanotechnology Research Center, Bilkent University, Ankara, Turkey; Institute of Materials Science and Nanotechnology, Bilkent University, 06800 Ankara, Turkey

Address all correspondence to Fatih Inci at **finci@bilkent.edu.tr**

(Received 19 October 2025; accepted 13 March 2026; published online: 27 April 2026)

Abstract

Sharp microneedle (MN) tips are crucial for reliable penetration; yet, tip resolution is limited by stereolithography (SLA) printing. We present an aspect ratio–guided printing angle optimization method in which the final layer, including MN tips, is aligned with the Z-axis. Optimal angles for conical, square, and hexagonal MNs of aspect ratios 2:1, 3:1, and 4:1 (75.96°, 80.54°, 82.88°) were calculated. This approach yielded 30% sharper tips than conventional orientations, with conical MNs consistently achieving ~20 µm diameters. By turning SLA's layer-by-layer limitation into an asset, this framework offers a predictive and transferable design tool for MN production.

Introduction

Microneedles (MNs) have emerged as a versatile platform for transdermal applications, since they can penetrate the underlying tissues with minimal pain and tissue deformation.[1] Their easy-to-use, self-administration potential, and ability to circumvent nociceptors make them particularly well-suited for drug and vaccine delivery.[2] Beyond therapeutics, MNs are increasingly being used as biosensing devices.[3,4] as the demand grew for effective and accessible delivery and diagnosis systems.[5,6] Therefore, precise control of MN geometry, especially tip sharpness, became a governing parameter in controlling both mechanical stability and penetration efficiency.[7]

High geometric precision required in MN tips has traditionally been achieved using microfabrication methods such as photolithography,[8] deep reactive ion etching (DRIE),[9] XeF_2-based etching,[10] and laser ablation.[11] While these processes provide excellent resolution and versatility with integrative systems such as a dicing-saw,[12] they are costly, cleanroom-dependent, and are not very flexible for design changes. In contrast, 3D printing has emerged as an adaptable and economically suitable alternative.[13] Among additive manufacturing methods, SLA offers rapid prototyping with customizable geometries.[14–16] However, SLA's intrinsic layer-by-layer nature imposes resolution limitations, particularly at the tip, where larger diameters significantly decrease the insertion efficiency.[17] It has been demonstrated in previous studies that printing angle can mitigate this limitation to some extent, revealing the great importance of geometric alignment in SLA resolution optimization.[4,18–22]

Tip sharpness, quantified by tip diameter, directly influences MN penetration efficacy, tissue response, and user comfort.[23] In SLA printing, however, the tip structure is limited by Z-axis resolution and needle geometry. Notably, when the terminal tip-defining layer is aligned with the build axis, the printer's maximum resolution can be directed at the tip. Printing angle, therefore, becomes not only a design choice but a controlling geometric variable that significantly affects tip fidelity. Previous studies explored printing angle effects mainly by testing common printing angles such as 30°, 45°, or 60°, and showed that aligning the tip closer to the build axis improved sharpness.[19] These findings motivated us to move beyond empirical screening and develop an aspect ratio–based framework that systematically determines the optimal Z-axis alignment through a predictive approach.

Here, we systematically investigated the effect of printing angle on SLA-fabricated MN tip geometry. Using square pyramidal MNs (aspect ratio 2:1), we compared fabrication at 0°, 45°, and the trigonometrically calculated optimal angle of 75.96°, which yielded a markedly reduced tip diameter. Extending this approach, optimal angles were determined for aspect ratios of 2:1, 3:1, and 4:1 (with a constant base width of 500 µm) as 75.96°, 80.54°, and 82.88°, respectively (Fig. 1). The resulting MNs were characterized using scanning electron microscopy (SEM) and 3D laser scanning microscopy (KEYENCE), mechanically tested using dynamic mechanical analysis (DMA), and evaluated for penetration efficiency using finite element simulations and *ex vivo* mice skin insertions. Our findings demonstrate that aligning the terminal MN layer with the Z-axis maximizes SLA's effective resolution, enabling the fabrication of significantly sharper tips. Importantly, this framework works for different geometries and aspect ratios, eliminating the need for trial-and-error angle screening. Collectively, this work establishes an aspect ratio–driven design framework that converts SLA's intrinsic layer-by-layer limitation into a resolution advantage, providing a predictive and low-cost strategy for fabricating sharper, reproducible MNs and advancing the broader field of 3D-printed microdevices.

Materials and methods

Microneedle design and fabrication

MNs with three geometries, conical, square pyramidal, and hexagonal pyramidal, were designed in Shapr3D (CAD software) with a fixed base width of 500 µm and heights of 1000, 1500, and 2000 µm (aspect ratios 2:1, 3:1, and 4:1). All MNs were fabricated as arrays on a cylindrical supporting base (patch) with a diameter of 15 mm and a height of 10 mm, each patch containing 139 needles. Models were exported as STL files and fabricated using a Creality Halot One SLA printer (CL-60, Creality, China) with a plant-based UV-curable resin (Anycubic, China). The resin consists primarily of acrylate-based monomers and crosslinkers, including 2,2′-(ethylenedioxy) diethyl diacrylate and triethylene glycol diacrylate (TEGDA), with glycerol propoxylated acrylates used to tailor viscosity.[24] Photopolymerization is initiated by phenyl bis(2,4,6-trimethylbenzoyl)-phosphine oxide under 405 nm UV illumination, yielding a crosslinked polymer network

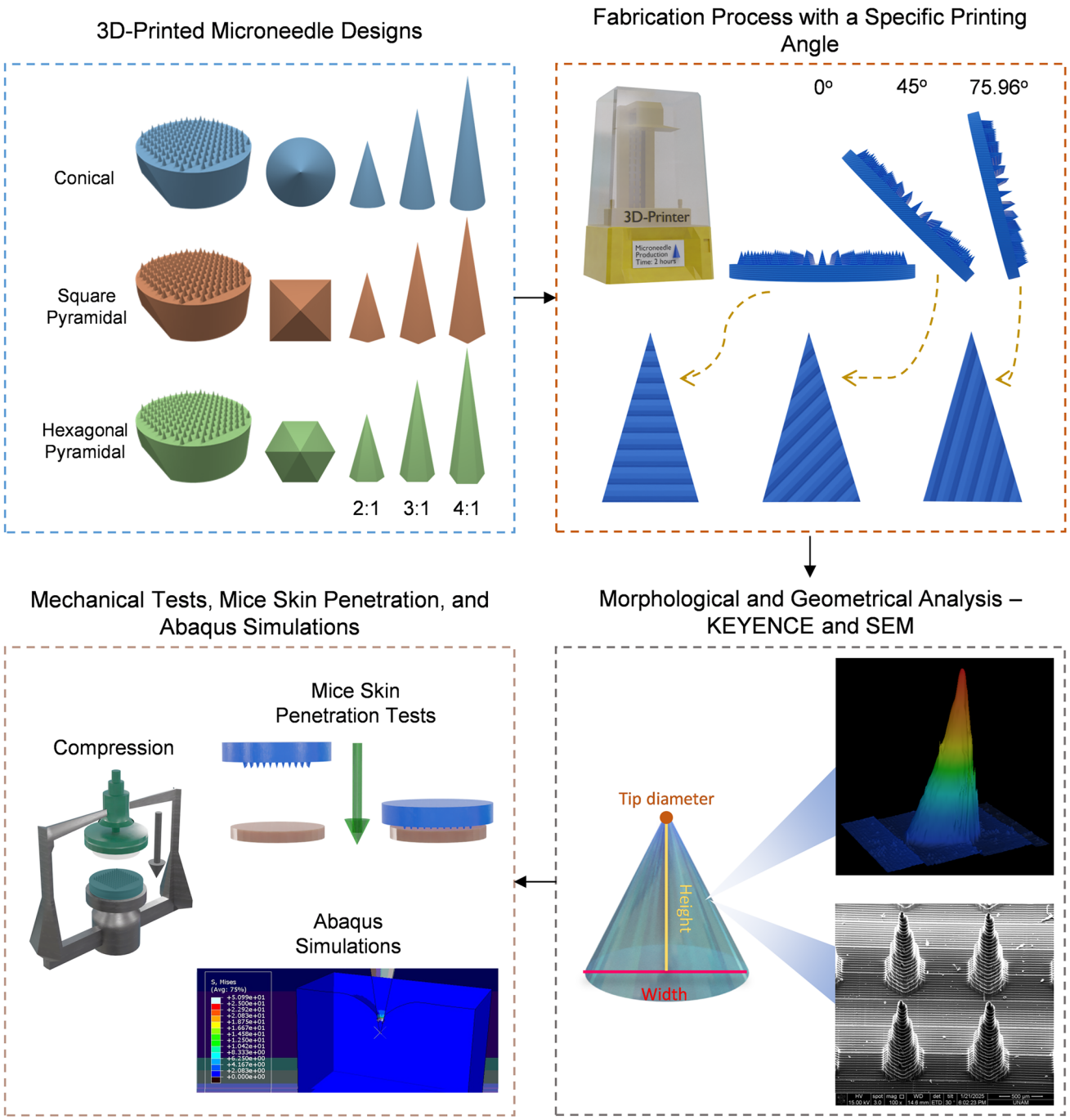

Figure 1. Workflow of the 3D-printed MN optimization process, from design and printing to morphological tests, mechanical performance, *ex vivo* penetration, and finite element simulations.

suitable for mechanically stable MN fabrication. Printing was performed with a 25 µm layer thickness, 2.5 s exposure time, and 40 s bottom layer exposure. To evaluate the effect of orientation, 2:1 square pyramidal MNs (1000 µm × 500 µm) were fabricated at 0° and 45° of printing angles, and compared with the calculated optimal angle of 75.96° (determined by the geometric relationship Θ = arctan (2 h/w), where h is the height and w is the base width, yielding arctan (4) = 75.96° for the 2:1 aspect ratio) obtained by aligning the tip region with the Z-axis. For all printing angles, the entire patch structure, including both the base and the MN array, was rotated as a single unit to ensure consistent boundary conditions across different orientations. Using this optimal angle, conical and hexagonal MNs with a 2:1 ratio were also fabricated. For higher aspect ratios, all three geometries were produced at their corresponding optimal angles: 80.54° (3:1) and 82.88° (4:1) (calculated following the same geometric principle). Fabricated MNs were rinsed in isopropyl alcohol (IPA) (5–10 min) and post-cured under 405 nm UV for 10 min using a UW-01 Washing and Curing Machine (Creality, China).

Geometrical and morphological analysis

All fabricated MNs were characterized using a 3D laser scanning microscope (VK-X100, Keyence, Japan) with a 10 × objective lens and a Z-axis step size of 1 µm. Surface models were reconstructed in VK Analyzer software to measure tip diameter, base width, and overall height. Printing efficiency was further calculated using Eq. 1.

$$Height\ Efficiency(\%) = \left(\frac{Measured\ Height}{Designed\ Height}\right) \times 100 \quad (1)$$

After these measurements, MNs with varying geometries and dimensions were characterized using SEM (FEI Quanta 200 F, FEI Company, USA) for morphology analysis. Prior to imaging, samples were coated with a 10 nm gold:palladium (Au:Pd) layer using a Gatan Model 682 Precision Etching and Coating System (PECS, Allest Instrument, USA). Samples were imaged both without tilt to examine base geometry and overall structure, and at a 30° tilt to visualize surface topography and tip morphology using 15 kV accelerating voltage and a 3.0 spot size.

Mechanical strength tests

Compression testing of the 3D-printed MNs was performed using DMA (TA Instruments – Q800, USA) under static loading conditions using a longitudinal loading approach (from the tip toward the base). A maximum force of 18 N was applied at a loading rate of 0.5 N/min at room temperature; this specific maximum load was selected as it represents the upper operational limit of the DMA instrument. The primary objective of this test was not to determine the ultimate material strength or the point of total destruction. Instead, it was designed as a comparative study to evaluate how different MN geometries and dimensions respond mechanically under identical printing parameters. By applying a standardized load, we aimed to assess the influence of geometric design on the mechanical integrity and functional stability of the arrays. Conventional printing angles (0° and 45°) were not included in this phase, as the focus was on examining the influence of tip diameter, aspect ratio, and geometry under optimized orientations, and on systematically assessing their mechanical strength. Force–displacement (plotted as force on the y-axis and displacement on the x-axis) curves were analyzed in GraphPad Prism to determine maximum displacement for each configuration. In addition, the displacement ratio (%) was calculated to normalize deformation relative to total needle height, using the following formula:

$$Displacement\ Ratio(\%) = \frac{Displacement}{Measured\ Height} \times 100 \quad (2)$$

Finite element simulation of skin penetration

Finite element analysis of MN penetration into human skin model was performed using the ABAQUS 2020 explicit solver. The specific scope of this computational study was to evaluate the theoretical penetration mechanics and stress distributions of the varying tip geometries, rather than to simulate the layer-by-layer fabrication artifacts of the SLA printing process. Three MN geometries were modeled with dimensions obtained from Keyence measurements (Table S1), ensuring the FE models accurately represented the structural fidelity and optimized tip profiles achieved through our angle-guided printing framework. As shown in Fig. S1, S2 each MN was positioned horizontally on top of the skin model, and a circular partition was introduced to refine the mesh locally. A reference point was assigned at the tip, where a point mass of 0.01 g was applied to simplify inertial effects and ensure stability. The MNs were assigned material properties corresponding to the Anycubic plant-based UV-curable resin used in fabrication. The resin was modeled as a homogeneous, isotropic material with a Young's modulus of 1300 MPa, a Poisson's ratio of 0.35, and a density of 1100 kg/m^3.[24]

The skin was represented as a three-layer structure consisting of the epidermis (70 µm), dermis (840 µm), and hypodermis (1000 µm) (Fig. S1).[25] Hyperelastic properties were assigned according to the Ogden model, with material parameters listed in Table S2. Due to natural variation in skin properties with age, sex, and anatomical site,[26] certain assumptions were made for consistency. The density of the *Epidermis* was set to 1300 kg/m^3, matching the primary protective component during penetration, which is the *Stratum Corneum*, while the *Dermis* and *Hypodermis* were both assigned densities of 1200 kg/m^3 to simplify model behavior without significantly affecting force outcomes.[27,28]

The external surfaces of the skin model were fixed with encastre boundary conditions (Fig. S3). Needle translation was restricted to the vertical (y) axis, and an insertion velocity

of 500 mm/s was applied at the reference point, reflecting dynamic MN insertion conditions reported in the literature.[29] Contact was modeled using general self-contact for stability and explicit surface-to-surface interactions between the MN and the skin partitions. After rupture, only tip region maintained the contact with the underlying tissue. Explicit dynamic integration was used, with total simulation times of 0.005 or 0.0025 s. For meshing, conical and hexagonal MN employed global seeds of 0.01 mm, while square MNs used 0.015 mm for stability. The skin mesh had a global seed of 0.15 mm. Edge refinement was applied at 200 seeds for conical, 300 for hexagonal, and 500 for square MNs. MNs were modeled with discrete rigid elements, and the skin with 3D stress elements from the explicit library. Element deletion was enabled via a subroutine that removed elements exceeding a von Mises stress of 60 MPa.[10] Enhanced hourglass control was enabled to stabilize the skin elements as they approached their failure threshold. No other meshing techniques were used in the simulation. Figure S4 shows the final mesh of the skin, conical needle, and the assembled system.

Skin penetration histological test

Histological visualization of the MN insertion sites was performed using trypan blue staining and hematoxylin–eosin (H&E) staining on mice skin. Animal studies were conducted under the approved ethical protocol (Protocol No. 2025/20) granted by the Bilkent University Animal Experiments Ethics Committee (BILHAYDEK). Eight-week-old female nude mice were terminated by exposure to a diethyl ether-filled container for 3–4 min, followed by cervical dislocation. The dorsal skin was excised, immersed in PBS enriched with penicillin–streptomycin, and mounted epidermis-side up on PBS-moistened Whatman paper. MNs were applied to the skin under thumb pressure for 60 s. In one sample, MNs were directly administered, whereas in the second sample, the skin was immersed in trypan blue solution for 30 s post-application to visualize the puncture sites. Tissues were fixed in 4% paraformaldehyde (PBS, pH 7.4) at 4℃ for 18 h, washed in PBS, and embedded in 3% agarose with the epidermal side facing upward. Agarose blocks were briefly chilled on ice and sectioned at 200 µm thickness using a vibratome. Free-floating sections were collected and processed for H&E staining: samples were stained with hematoxylin (10 min), rinsed in tap water, counterstained with 0.5% eosin (2 min), dehydrated through graded ethanol (50–100%), cleared in isopropanol, and mounted with glycerol. For top-view observation, a 1% (w/w) Nile red stock solution was first prepared and then added to a 5% (w/v) sucrose solution at a 1:100 (v/v) ratio. The resulting mixture was drop-cast onto the MN surfaces and air-dried. The coated MNs were then inserted into the mice skin, and fluorescence microscopy was performed from the top view to observe the penetration sites and Nile red distribution within the tissue.

Results and discussions

In order to initiate the aspect ratio-specific strategy, we first examined the effect of printing angle on tip diameter using square pyramidal MNs with a 2:1 aspect ratio. Geometric fidelity and tip sharpness were quantitatively assessed with Keyence VK X100 [Fig. 2a(i-iii)]. The target design was 1000 µm height and 500 µm width. As expected for SLA, the measured heights were slightly lower than designed, reaching 857.64 ± 11.26 µm at 0° of printing angle, 840.90 ± 9.48 µm at 45° of printing angle, and 837.36 ± 5.18 µm at 75.96° of printing angle (Fig. 2a(iv)). The dimensional accuracy loss compared to design was within 15–16% with only a ~2% difference between 0° and optimized 75.96° of printing angles. Widths were consistently larger than 500 µm (532–633 µm) due to overcuring and light scattering in the horizontal plane (Fig. 2a(v)), an intrinsic limitation of SLA that is well documented. These dimensional variations confirmed the expected anisotropy between XY- and Z-axis resolution.

Most importantly, tip sharpness improved dramatically with the optimized orientation. Tip diameter decreased from 47.94 ± 1.75 µm at 0° of printing angle to 41.24 ± 1.41 µm at 45° of printing angle, and further to 32.86 ± 2.51 µm at 75.96° of printing angle, representing a 31.5% reduction compared to 0° of printing angle and 20.3% compared to 45° of printing angle (Fig. 2a(vi)). This clear improvement demonstrates that aligning the final layer forming the MN tip with the Z-axis transforms SLA's layer resolution into a distinct advantage. Although a minor loss in height accuracy was observed (~2%), this deviation is minor compared to the substantial gains in tip sharpness. These findings validate the central premise that tip orientation is the dominant factor for exploiting SLA resolution at the microscale. Accordingly, all subsequent MN designs in this study were fabricated at aspect ratio-specific optimized angles to ensure maximum sharpness.

To move beyond angle optimization in single geometry and aspect ratio, we next assessed how shape and aspect ratio modulate both dimensional fidelity and tip sharpness when the tip-forming layer is aligned with the build (Z) axis. In this part, to investigate the effect of MN geometry and aspect ratio, we fabricated conical, square pyramidal, and hexagonal pyramidal MNs at fixed width (500 µm) and target heights of 1000 µm (2:1), 1500 µm (3:1), and 2000 µm (4:1). For each aspect ratio, we used trigonometric angle that makes the final, tip-forming layer parallel to the Z-axis (75.96°, 80.54°, and 82.88° of printing angles for 2:1, 3:1, and 4:1, respectively). In practice, the optimized angle is primarily aspect ratio-dependent, and any geometry-specific deviations are small at the apex scale considered here.

At 2:1 (Fig. 2b(i-iii)), the square pyramidal MNs retained the greatest height (837.36 ± 5.18 µm, 83.7% of target), followed by conical (815.7 ± 5.50 µm, 81.6%), and hexagonal pyramidal (812.05 ± 5.68 µm, 81.2%) (Fig. 2b(iv)). As the aspect ratio increased, the conical geometry exhibited a clear advantage: at 3:1, it reached 1287.88 ± 15.29 µm (85.9% of target) versus 1263.51 ± 5.96 µm (84.2%) for square pyramidal

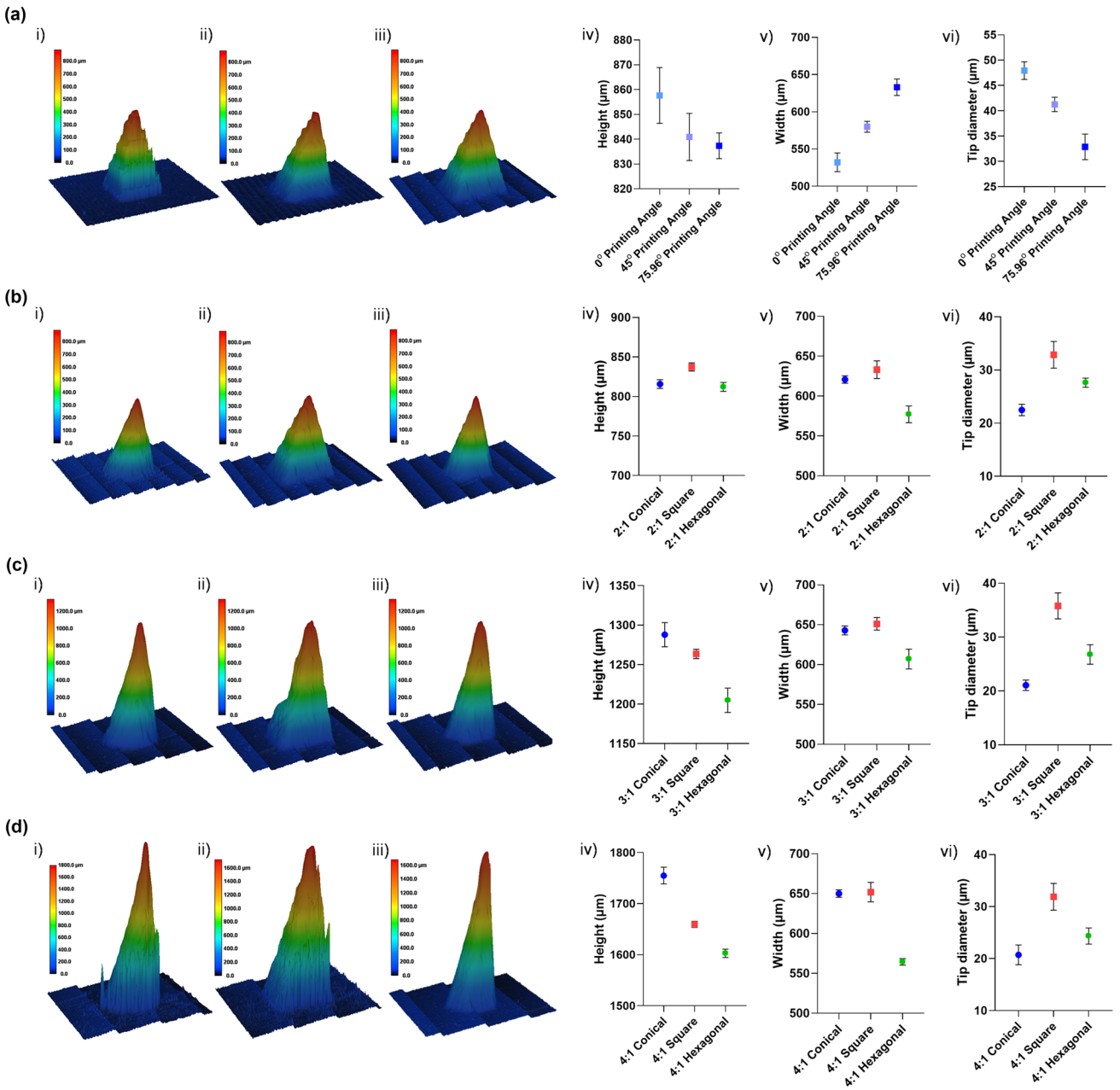

Figure 2. Keyence VK X100 analyses of 3D-printed MNs with different aspect ratios and geometries. (a) Square pyramidal MNs (aspect ratio 2:1) fabricated at three different printing angles: (i) 0°, (ii) 45°, and (iii) 75.96°. (iv–vi) Corresponding measurements showing comparisons of MN height, base width, and tip diameter ($n = 5$). (b–d) Comparison of MNs with an aspect ratio of 2:1 (b), 3:1 (c), and 4:1 (d) fabricated in three geometries: (i) conical, (ii) square pyramidal, and (iii) hexagonal pyramidal. (iv–vi) Keyence measurements of MN height, base width, and tip diameter for each geometry ($n = 5$).

and 1204.82 ± 15.40 μm (80.3%) for hexagonal pyramidal (Fig. 2c(iv)). At 4:1, it further increased to 1754.90 ± 16.43 μm (87.7%) versus 1659.56 ± 6.18 μm (83.0%) and 1602.68 ± 8.07 μm (80.1%) for square and hexagonal designs (Fig. 2d(iv)). Thus, height retention improves with aspect ratio in conical MNs (from 81.6 to 87.7%), while it plateaus or declines in faceted geometries. This trend is likely due to the more uniform distribution of cure-shrinkage stresses and reduced peel-induced bending along the continuously tapering cone. On the other hand, flat facets and sharp vertices in square/hexagonal shapes introduce stress localization and non-uniform contraction under layer-wise constraints, leading to measurable loss of height at high aspect ratios.

In addition to height, tip sharpness (quantified by tip diameter) consistently favored the conical geometry across aspect ratios. At 2:1, conical MNs exhibited a tip diameter of 22.48 ± 1.06 μm, compared to 32.86 ± 2.52 μm for square

pyramidal and 27.62 ± 0.85 µm for hexagonal pyramidal designs, correspondingly sharper as 31.6% and 18.6%, respectively (Fig. 2b(vi)). At 3:1, the conical tip decreased to 21.05 ± 0.96 µm, whereas the square and hexagonal pyramidal tips measured 35.79 ± 2.41 µm and 26.77 ± 1.80 µm, respectively (41.2% and 21.4% smaller tip) (Fig. 2c(vi)). This trend continued at 4:1, with the conical tip maintaining the smallest diameter (20.70 ± 1.90 µm) compared to 31.88 ± 2.58 µm (square) and 24.33 ± 1.55 µm (hexagonal) (35.1% and 14.9% smaller tip) (Fig. 2d(vi)). Mechanistically, it can be claimed that the cone's smooth shape reduces lateral voxel bleed and overexposure issues near edges, enabling tighter energy confinement at the apex during photopolymerization. In contrast, multi-edged facets introduce edge scattering and local overcuring, which broaden the tip. Together with the aspect ratio-dependent Z-axis alignment, this explains the advantage of conical MNs in tip diameter. Finally, consistent with SLA physics, widths exceeded the designed 500 µm due to XY-plane overcuring and light scattering: this highlights that, despite intrinsic XY limitations, tip sharpness can be systematically controlled through aspect ratio–guided Z-axis alignment.

To complement quantitative profilometry, SEM was used to assess the surface morphology and geometric fidelity of conical, square pyramidal, and hexagonal MNs across aspect ratios (Fig. 3(a)). Base geometries were preserved with high fidelity; corner features remained well defined though slightly rounded, reflecting the voxel resolution of SLA. Height scaling with aspect ratio was consistently with Keyence measurements (Fig. 3a(i-iii)). Sidewalls displayed characteristic layer lines, whereas the tip regions appeared smoother and more continuous, demonstrating the effect of aspect-ratio guided Z-axis alignment in improving tip definition. SEM observations corroborated profilometry results, confirming conical tips were consistently the sharpest, followed by hexagonal and square designs. Minor surface irregularities were occasionally observed as randomly distributed and attributed to sample preparation rather than fabrication process. Overall, SEM provided visual confirmation that optimized orientation produces MNs with sharp tips and robust structural fidelity across geometries.

Following SEM analysis, the compressive performance of MNs with different geometries and aspect ratios was evaluated (Fig. 3(b–e)). A static force up to 18 N was applied in 0.5 N/min increments per minute, and displacement was recorded to assess the deformation resistance. At 2:1, square pyramidal MNs showed the lowest deformation (76.14 µm, 9.09%) compared to hexagonal (99.59 µm, 12.26%) and conical (106.95 µm, 13.12%) (Fig. 3(b)). This reflects the stabilizing effect of the broader base and corner in the square design, while the tapered conical structure, though sharper, concentrated stress at the apex and deformed more readily. Force–displacement curves confirmed that square MNs maintained the stiffest, most linear response, while conical and hexagonal geometries displayed nonlinear deviations beyond ~12 N, consistent with the onset of lateral buckling.

At 3:1, displacement ratios increased across all designs, reflecting reduced stiffness in taller MNs. Conical MNs deformed most (189.11 µm, 14.68%), followed by hexagonal (167.35 µm, 13.89%) and square (119.18 µm, 9.43%) (Fig. 3(c)). A crossover in the conical and hexagonal curves beyond 9 N indicated progressive instability in the conical profile. Moreover, this crossover also indicates a shift toward greater structural instability in the conical MNs at higher forces due to their tapered profile and sharper tip. At higher static force, both conical and hexagonal MNs exhibited nonlinear formation, such as axial buckling, which becomes more dominant as the MN height increases. At 4:1, deformation peaked, conical MNs reached 385.54 µm (21.96%), versus hexagonal (327.42 µm, 20.43%) and square (308.43 µm, 18.58%) (Fig. 3(d)). Conical MNs exhibited early instability (steep displacement at ~2 N), while square and hexagonal designs showed small plateau-like irregularities at 2–6 N, likely due to local buckling or interlayer slip.

Importantly, despite the buckling and deformation observed at higher forces and aspect ratios, no catastrophic fracture (shattering) was recorded up to the maximum load of 18 N across any of the tested designs. Instead, the 3D-printed resin MNs exhibited elastic–plastic deformation (blunting or slight bending) rather than brittle fracture. From a clinical safety perspective, this is a significant advantage: MNs that maintain their structural integrity or deform slightly under extreme stress are far less likely to leave sharp polymeric fragments within the skin tissue compared to brittle alternatives.

Previous studies have established that MN geometry fundamentally dictates the trade-off between insertion mechanics and structural integrity. For instance, literature comparing various tip shapes has demonstrated that pyramidal designs generally offer superior mechanical strength due to their broader base and edge-dominated stress distribution,[30] whereas conical geometries minimize tissue insertion forces owing to their smooth, continuously tapered profiles. Consistent with these foundational principles, our evaluation demonstrated that square pyramidal MNs consistently exhibited the greatest compressive robustness, with smoother, more linear load–displacement profiles. Conical MNs, by contrast, provided the sharpest tips but were more prone to instability at higher aspect ratios. Hexagonal MNs showed intermediate performance, representing a compromise between sharpness and strength (Fig. 3(e)). These results highlight the importance of geometry selection: conical MNs are favorable for efficient penetration, square MNs for mechanical durability, and hexagonal MNs when a balance of both properties is desired. While the current study focuses on the compressive behavior of rigid, solid resin MNs, which dictates the primary failure modes during initial skin insertion, future applications utilizing flexible or elastomeric resins for conformable wearable patches will also necessitate comprehensive tensile testing. Evaluating the tensile properties of such flexible arrays will be essential to ensure they can withstand the stretching, shearing, and peeling forces associated with dynamic skin movement and patch removal.

Following mechanical tests, the effect of MN geometry and tip diameter on insertion efficiency was further evaluated using

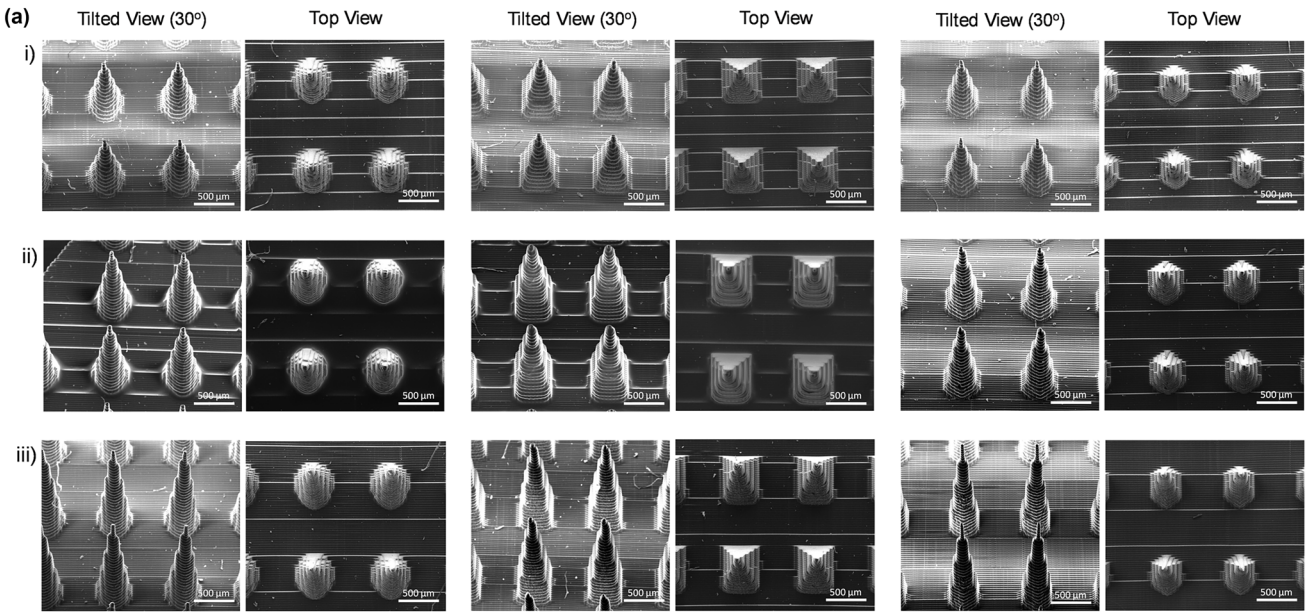

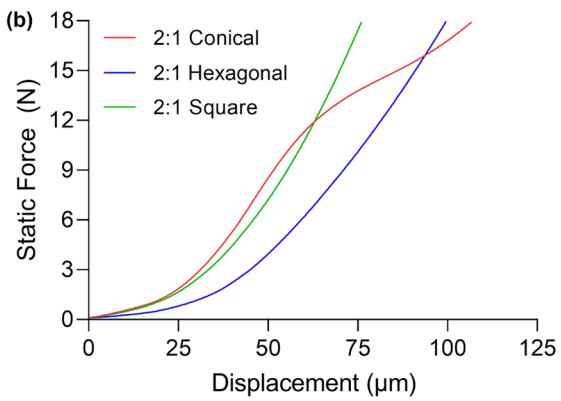

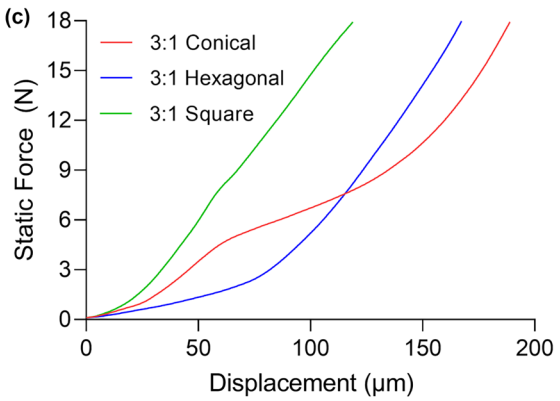

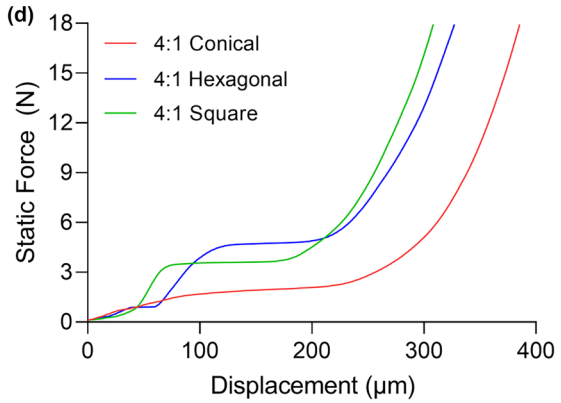

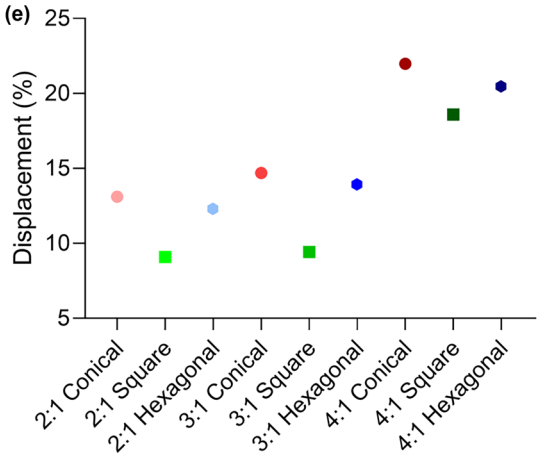

Figure 3. (a) SEM images of MNs with aspect ratios of (i) 2:1, (ii) 3:1, and (iii) 4:1. For each aspect ratio, conical, square pyramidal, and hexagonal pyramidal geometries are shown from left to right. Each MN was imaged both from the top view and at a 30° stage tilt to evaluate base integrity and tip morphology. (b–d) Force–displacement curves obtained from static compression tests of MNs with aspect ratios of 2:1 (b), 3:1 (c), and 4:1 (d), comparing conical, square pyramidal, and hexagonal pyramidal geometries. (e) Comparison of displacement ratio (%) values across all aspect ratios and geometries, calculated by normalizing total displacement to measured MN height.

finite element simulations (Abaqus). Crucially, the objective of these simulations was to isolate the biomechanical impact of the optimized tip morphologies (e.g., ~20 μm diameters) and aspect ratios on tissue penetration, rather than to model the layer-by-layer artifacts of the SLA printing process. Critical displacement (Dc), was defined as the axial tip displacement at the moment of first epidermal element deletion under a von Mises stress-based failure criterion (60 MPa). As shown in (Fig. 4(a–d)), increasing the MN aspect ratio was found to consistently reduce the Dc, attributable to smaller tip diameters and steeper apex profiles. Therefore, higher aspect ratios concentrate contact pressure more efficiently, suggesting that sharper and slenderer MNs require less deformation for successful skin insertion. For instance, increasing tip diameter from approximately 20 μm (conical) to 35 μm (square) resulted in nearly an 80% increase in Dc. This is a result of how the stress becomes focused at the tip of the needle interface. Conical tips, with gradually tapering profiles, focused stress more effectively at the apex and achieved rupture at lower deformation, while the flat-end and edge-dominated profiles of square and hexagonal overall deformation. This underscores the substantial impact of tip sharpness on the penetration threshold.

One notable trend was that higher aspect ratio MNs generally exhibited lower Dc values, even at similar nominal tip diameters. Under the rigid-needle assumption, this effect arises from contact mechanics (apex stress focusing, reduced effective contact area) rather than structural bending. Because our angle-guided framework successfully aligns the MN tips with the Z-axis to eliminate significant printing artifacts, the FE models utilized the smooth, physical dimensions verified by Keyence microscopy. Therefore, simulating 'non-optimal' or stepped geometries was outside the scope of this biomechanical assessment. Furthermore, deformation modes such as lateral deflection or buckling are not presented in this simulation, as the structural integrity and failure modes of the as-printed arrays were already addressed and validated experimentally in our DMA compression tests. These results highlighted a dual effect of aspect ratio: it sharpens the geometry (favoring lower Dc), but in real MNs could also reduce mechanical robustness due to increased compliance. Therefore, aspect ratio and geometry must be optimized with both contact efficiency (Dc) and experimental deformation response in view for reliable, reproducible penetration.

Moreover, the penetration force (F_p) is defined here as the reaction force required at the tip reference point at the instant of epidermal rupture.[27] This metric depends on skin properties and MN geometry. For conical MNs, which was preferred due to their best tip diameter properties and tapered structures, increasing the aspect ratio from 2:1 to 4:1 led to a ~35% rise in Fp while Dc decreased (Fig. 4(e–f)). Thus, sharper tips lowered displacement to failure (Dc) but concentrated stresses raised the reaction force (Fp), especially under high-rate loading (Fig. S5-7). Accordingly, Dc serves as the primary efficiency metric, while Fp reflects setup-dependent force response.

These simulation results together highlight the critical influence of MN geometry and aspect ratio on insertion mechanics. Sharper tips and higher aspect ratios consistently reduce Dc (displacement to epidermal failure) under the rigid-needle contact model, facilitating easier penetration. Force trends are rate- and boundary-condition dependent in this setup and should be read comparatively. Therefore, a compromise between mechanical stability and tip sharpness is required for optimum MN performance. Conical MNs, which consistently exhibited the lowest critical displacement for each aspect ratio due to their improved tip sharpness in simulation results, were subsequently selected for validation using *ex vivo* mice skin penetration experiments.

Microscopy analyses revealed punctate defects at the epidermal surface, corresponding to MN penetration sites, along with channels extending through epidermal-dermal interface (Fig. 4(g–h)). Trypan blue allowed for rapid macroscopic visualization of puncture sites, while H&E staining revealed the microscopic architecture of insertion channels crossing the epidermis–dermis interface. Complementary Nile red fluorescence imaging showed localized emission confined to the puncture regions, confirming that the fluorescent dye penetrated through the created microchannels and accumulated along the insertion paths (Fig. 4(i)). These findings indicate that the fabricated MNs reproducibly created pores with ~40% insertion depth, demonstrating their suitability for transdermal applications and further studies on drug delivery or biomarker sampling.

Together, these findings demonstrate that the aspect ratio–guided printing angle approach effectively overcomes the intrinsic tip-resolution limitation of SLA. By orienting the tip-forming layer along the Z-axis, MNs with tip diameters as small as ~20 μm were reproducibly fabricated. Among the examined designs, conical MNs exhibited the best fabrication performance, successfully breaching skin tissue in *ex vivo* tests. Overall, this strategy eliminates the need for empirical angle screening and can be readily extended to various geometries and aspect ratios, offering a robust and scalable route for high-fidelity SLA fabrication of MNs.

Conclusion

In this work, we introduced an aspect-ratio-driven printing angle optimization that leverages the additive manufacturing limitation of SLA into an advantage for MN fabrication. By aligning the tip-forming layer with the Z-axis, more than a 30% increase in tip sharpness was observed in comparison to conventional orientations. Furthermore, conical MNs consistently provided the sharpest profiles (~20 μm). High geometric accuracy was confirmed using SEM, while mechanical tests revealed a balance between penetration performance and structural strength: conical MNs had sharper tips but were less stable under load, while square MNs exhibited higher compressive strength, and hexagonal MNs offered intermediate stability. Finite element analyses revealed that larger aspect ratios increased stress concentration and reduced critical displacement, facilitating penetration. *Ex vivo* mouse skin tests

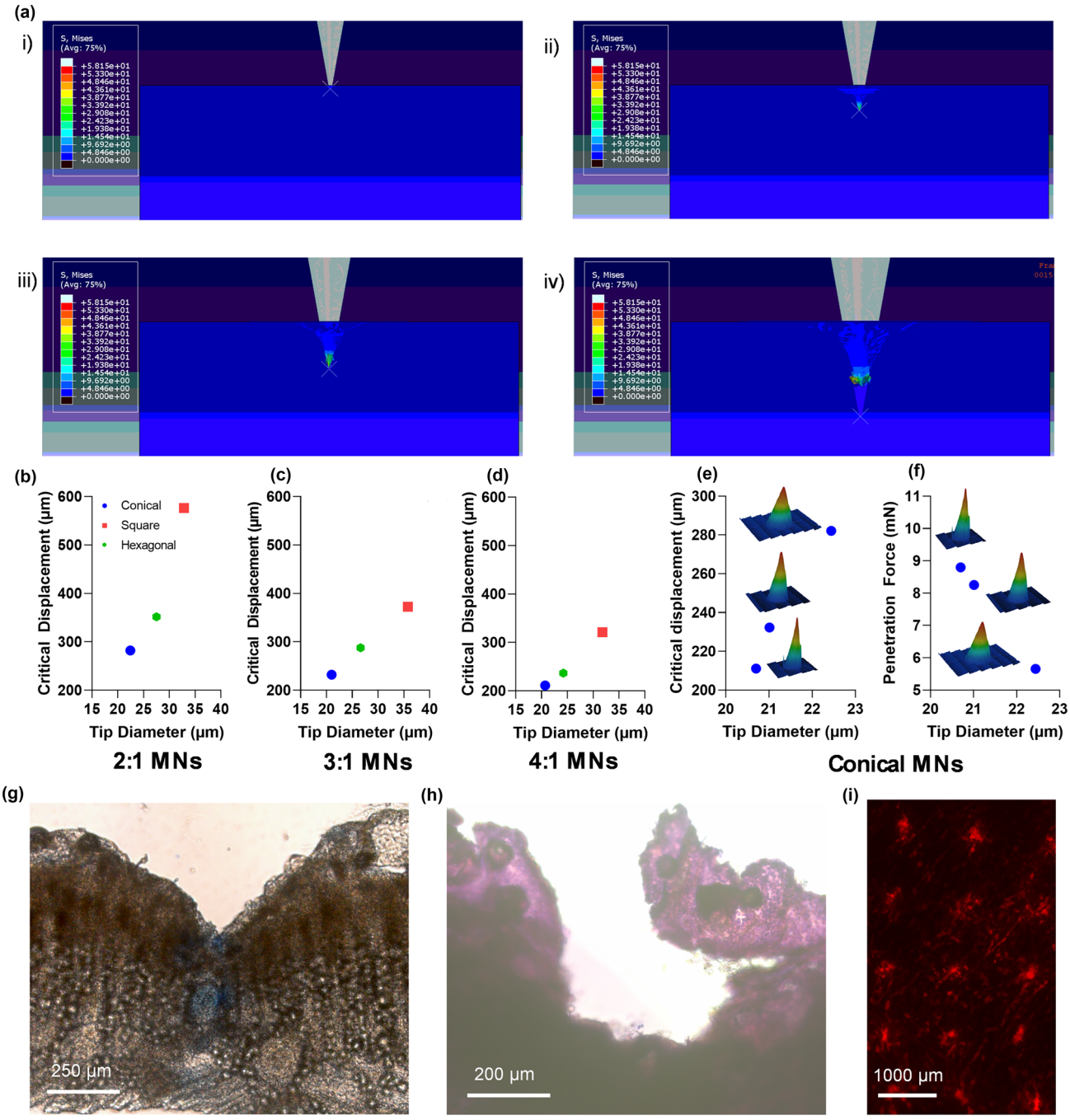

Figure 4. (a) Simulation setup and deformation model during MN insertion. (b–d) Critical displacement values for conical, square pyramidal, and hexagonal MNs with aspect ratios of 2:1 (b), 3:1 (c), and 4:1 (d). (e) Dc values for conical MNs with increasing aspect ratios. (f) Fp values for conical MNs with increasing aspect ratios. (g–i) Representative histological images of MN penetration in mice skin, showing trypan blue (g) and H&E (h) cross-sectional staining of insertion channels, and Nile red (i) top-view fluorescence indicating localized dye distribution around puncture sites.

confirmed penetration of approximately 40% of the needle length, consistent with *ex vivo* ranges reported in the literature, demonstrating the translational value of the proposed approach. While the rigid-needle assumption and the use of *ex vivo* tissues in the simulation introduce some limitations, the combination of experimental and computational results strongly supports the design methodology. Looking forward, this framework may be extended to other printing platforms and material systems, and further complemented by large-area statistical or full-field metrology approaches (e.g., CAD-to-scan deviation mapping using software such as Geomagic or Zeiss Inspect) in high-throughput manufacturing and quality-control contexts.

Additionally, future computational studies could employ reverse engineering of these full-field 3D scans to simulate the exact 'as-printed' geometries. Simulating the actual printouts at various non-optimal angles would capture layer-by-layer artifacts and stair-stepping effects, providing deeper insights into how specific manufacturing deviations influence localized stress distributions and penetration mechanics. Overall, this work demonstrates a predictive and cost-effective paradigm that maximizes the resolution capabilities of SLA and guides geometry/orientation choices. Beyond MNs, the same principle can be applied to the fabrication of other high-aspect-ratio biomedical and microfluidic devices, potentially expanding the translational utility of SLA in device fabrication.

Acknowledgments

Dr. Fatih Inci gratefully acknowledges being selected as a Spring 2025 MRS Communications Early Career Distinguished Presenter and appreciates the invitation to contribute to the corresponding special issue of MRS Communications. Dr. Inci gratefully thanks the support of the Scientific and Technological Research Council of Turkey (TÜBİTAK) through the 2232 International Fellowship for Outstanding Researchers (Project No: 118C254). The authors are solely responsible for the content of this publication, and the financial support provided by TÜBİTAK does not imply its scientific endorsement. Dilsad Taydas also acknowledges support from TÜBİTAK 2211 National PhD Scholarship Program. Dr. Inci further acknowledges TÜBİTAK Incentive Award, the Outstanding Young Scientists Award Program (TÜBA-GEBİP) from Turkish Academy of Sciences, Young Scientist Award (BAGEP) from the Science Academy, TÜSEB Aziz Sancar Incentive Award, Dr. Nejat Eczacibasi Medicine Incentive Award, and the Science Award from the İzmir Biomedicine and Genome Center (IBG). The authors would like to thank Assistant Professor Onur Cizmecioglu for kindly providing the animal skin samples used in this study and for his valuable assistance in the related experimental procedures.

Author contributions

Emre Ece developed the main concept of the study, planned and conducted experiments, analyzed the data, and wrote the manuscript. Shammas Mohamed, Eylul Gulsen Yilmaz, Dilsad Taydas, Nedim Haciosmanoglu contributed to the experimental work, data interpretation, and preparation of the manuscript. Fatih Inci developed the conceptualization of the study, contributed to experimental design, and data evaluation, supervised the research, revised the manuscript, validated all results, and provided funding support. All authors read and approved the final version of the manuscript.

Funding

This study is supported by TÜBİTAK through the 2232 International Fellowship for Outstanding Researchers (Project No: 118C254).

Data availability

The data generated and analyzed during the current study are available from the corresponding author upon reasonable request.

Declarations

Conflict of interest

The authors declare that they do not have any conflict of interest.

Supplementary Information

The online version contains supplementary material available at https://doi.org/10.1557/s43579-026-00955-6.

References

1. M.T.C. McCrudden, E. McAlister, A.J. Courtenay et al., Microneedle applications in improving skin appearance. Exp. Dermatol. **24**, 561–566 (2015). https://doi.org/10.1111/exd.12723
2. Y.-C. Kim, J.-H. Park, M.R. Prausnitz, Microneedles for drug and vaccine delivery. Adv. Drug Deliv. Rev. **64**, 1547–1568 (2012). https://doi.org/10.1016/j.addr.2012.04.005
3. E. Ece, I. Eş, F. Inci, Microneedle technology as a new standpoint in agriculture: treatment and sensing. Mater. Today **68**, 275–297 (2023). https://doi.org/10.1016/j.mattod.2023.07.002
4. E. Ece, N. Hacıosmanoğlu, M.A. Güngen et al., In-Field Detection of Plant Pathogens Using Three-Dimensional-Printed Microneedles and a Portable Platform. ACS Sens. **10**, 9397–9410 (2025). https://doi.org/10.1021/acssensors.5c02361
5. E.G. Yilmaz, E. Ece, Ö. Erdem et al., A Sustainable Solution to Skin Diseases: Ecofriendly Transdermal Patches. Pharmaceutics **15**, 579 (2023). https://doi.org/10.3390/pharmaceutics15020579
6. N. Hacıosmanoğlu, E. Ece, F. Inci, A wearable 3D-printed hollow microneedle device for pressure-driven interstitial fluid collection and testing. Lab Chip (2026). https://doi.org/10.1039/D5LC00657K
7. O. Olatunji, D.B. Das, M.J. Garland et al., Influence of Array Interspacing on the Force Required for Successful Microneedle Skin Penetration: Theoretical and Practical Approaches. J. Pharm. Sci. **102**, 1209–1221 (2013). https://doi.org/10.1002/JPS.23439
8. Z. Chen, L. Ren, J. Li et al., Rapid fabrication of microneedles using magnetorheological drawing lithography. Acta Biomater. **65**, 283–291 (2018). https://doi.org/10.1016/j.actbio.2017.10.030
9. Y. Liu, P.F. Eng, O.J. Guy et al., Advanced deep reactive-ion etching technology for hollow microneedles for transdermal blood sampling and drug delivery. IET Nanobiotechnol. **7**, 59–62 (2013). https://doi.org/10.1049/iet-nbt.2012.0018
10. I. Eş, A. Kafadenk, M.B. Gormus, F. Inci, Xenon difluoride dry etching for the microfabrication of solid microneedles as a potential strategy in transdermal drug delivery. Small **19**, 2206510 (2023). https://doi.org/10.1002/smll.202206510
11. T. Evens, O. Malek, S. Castagne et al., Controlling the geometry of laser ablated microneedle cavities in different mould materials and assessing the replication fidelity within polymer injection moulding. J. Manuf. Process. **62**, 535–545 (2021). https://doi.org/10.1016/j.jmapro.2020.12.035
12. I. Eş, A. Kafadenk, F. Inci, A high-precision method for manufacturing tunable solid microneedles using dicing saw and xenon difluoride-induced dry etching. J. Mater. Process. Technol. **325**, 118268 (2024). https://doi.org/10.1016/j.jmatprotec.2023.118268
13. R. Li, L. Zhang, X. Jiang et al., 3D-printed microneedle arrays for drug delivery. J. Control. Release **350**, 933–948 (2022). https://doi.org/10.1016/j.jconrel.2022.08.022
14. C. Heuer, J. Preuß, T. Habib et al., 3D printing in biotechnology—an insight into miniaturized and microfluidic systems for applications from cell culture to bioanalytics. Eng. Life Sci. **22**, 744–759 (2022). https://doi.org/10.1002/elsc.202100081

15. W. Li, M. Wang, H. Ma et al, Stereolithography apparatus and digital light processing-based 3D bioprinting for tissue fabrication. iScience 26:106039 (2023) https://doi.org/10.1016/j.isci.2023.106039
16. N. Hacıosmanoğlu, M.A. Güngen, E.G. Yilmaz et al., SpAi: A machine-learning supported experimental workflow for high-throughput spheroid production and analysis. Biosens. Bioelectron. X **23**, 100588 (2025). https://doi.org/10.1016/j.biosx.2025.100588
17. P. Khanna, K. Luongo, J.A. Strom, S. Bhansali, Sharpening of hollow silicon microneedles to reduce skin penetration force. J. Micromech. Microeng. **20**, 045011 (2010). https://doi.org/10.1088/0960-1317/20/4/045011
18. S.N. Economidou, C.P. Pissinato Pere, M. Okereke, D. Douroumis, Optimisation of design and manufacturing parameters of 3D printed solid microneedles for improved strength, sharpness, and drug delivery. Micromachines **12**, 117 (2021). https://doi.org/10.3390/MI12020117
19. S. Choo, S. Jin, J. Jung, Fabricating high-resolution and high-dimensional microneedle mold through the resolution improvement of stereolithography 3D printing. Pharmaceutics **14**, 766 (2022). https://doi.org/10.3390/pharmaceutics14040766
20. E. Mathew, G. Pitzanti, A.L. Gomes dos Santos, D.A. Lamprou, Optimization of printing parameters for digital light processing 3D printing of hollow microneedle arrays. Pharmaceutics **13**, 1837 (2021). https://doi.org/10.3390/pharmaceutics13111837
21. J. Jeong, J. Park, S. Lee, 3D printing fabrication process for fine control of microneedle shape. Micro Nano Syst. Lett. **11**, 1 (2023). https://doi.org/10.1186/s40486-022-00165-4
22. M. Razzaghi, M. Akbari, The effect of 3D printing tilt angle on the penetration of 3D-printed microneedle arrays. Micromachines **14**, 1157 (2023). https://doi.org/10.3390/mi14061157
23. E.Z. Loizidou, N.T. Inoue, J. Ashton-Barnett et al., Evaluation of geometrical effects of microneedles on skin penetration by CT scan and finite element analysis. Eur. J. Pharm. Biopharm. **107**, 1–6 (2016). https://doi.org/10.1016/j.ejpb.2016.06.023
24. Anycubic Anycubic - Plant-Based UV Resin 2.0. https://store.anycubic.com/products/plant-based-uv-resin?variant=45619242336418. Accessed 10 Jan 2026
25. R.B. Groves, S.A. Coulman, J.C. Birchall, S.L. Evans, Quantifying the mechanical properties of human skin to optimise future microneedle device design. Comput. Methods Biomech. Biomed. Eng. **15**, 73–82 (2012). https://doi.org/10.1080/10255842.2011.596481
26. A.K. Dąbrowska, F. Spano, S. Derler et al., The relationship between skin function, barrier properties, and body-dependent factors. Ski. Res. Technol. **24**, 165–174 (2018). https://doi.org/10.1111/srt.12424
27. S. Chen, N. Li, J. Chen, Finite element analysis of microneedle insertion into skin. Micro Nano Lett. **7**, 1206–1209 (2012). https://doi.org/10.1049/mnl.2012.0585
28. A.H. Sabri, Z. Cater, J. Ogilvie et al., Characterisation of mechanical insertion of commercial microneedles. J. Drug Deliv. Sci. Technol. **58**, 101766 (2020). https://doi.org/10.1016/j.jddst.2020.101766
29. S.A. Ranamukhaarachchi, B. Stoeber, Determining the factors affecting dynamic insertion of microneedles into skin. Biomed. Microdev. **21**, 100 (2019). https://doi.org/10.1007/s10544-019-0449-y
30. J.W. Lee, J.-H. Park, M.R. Prausnitz, Dissolving microneedles for transdermal drug delivery. Biomaterials **29**, 2113–2124 (2008). https://doi.org/10.1016/j.biomaterials.2007.12.048

Publisher's Note Springer Nature remains neutral with regard to jurisdictional claims in published maps and institutional affiliations.

Springer Nature or its licensor (e.g. a society or other partner) holds exclusive rights to this article under a publishing agreement with the author(s) or other rightsholder(s); author self-archiving of the accepted manuscript version of this article is solely governed by the terms of such publishing agreement and applicable law.